ACS Photonics

pubs.acs.org/journal/apchd5 Article

Driving Orbital Magnetism in Metallic Nanoparticles through Circularly Polarized Light: A Real-Time TDDFT Study

Rajarshi Sinha-Roy,* Jérôme Hurst, Giovanni Manfredi,* and Paul-Antoine Hervieux

Cite This: *ACS Photonics* 2020, 7, 2429−2439 Read Online

ACCESS | Metrics & More | Article Recommendations | Supporting Information

ABSTRACT: Transfer of angular momentum from helicity-controlled laser fields to a nonmagnetic electronic system can lead to the creation of magnetization. The underlying mechanism in metallic nanoparticles has been studied using different theoretical approaches. However, an understanding of the dynamics using an orbital-based quantum-mechanical method within the many-body theoretical framework is still due. To this end, the real-time formulation of time-dependent, density-functional theory is used to study induced orbital magnetism in metallic nanoparticles (clusters) excited by circularly polarized light. The nanoparticles are described by a spherical jellium model on a real-space grid. The polarized laser field gives rise to an angular momentum and, hence, a magnetic moment, which is maximum at the surface plasmon frequency of the nanoparticle, revealing that this is a resonant plasmonic effect. The primary contribution to the magnetic moment comes from surface currents generated by the plasmonic field, although some bulk contributions due to the quantum-mechanical nature of the system (Friedel oscillations) still persist. We compare several nanoparticles of K, Na, and Au having the same size and excited at their respective plasmon frequencies and show that the generated magnetic moment per energy pumped into the system is maximum for K and minimum for Au. A similar trend is observed for nanoparticles of the same chemical species but different sizes.

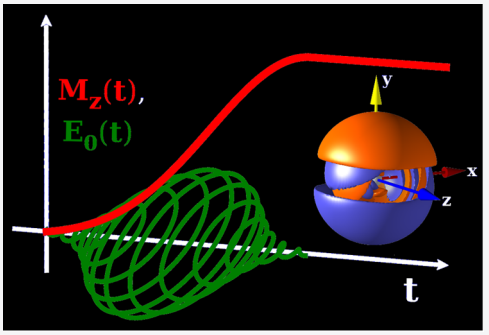

KEYWORDS: *magneto-optical response, inverse Faraday effect, time-dependent density-functional theory, plasmon, orbital angular momentum, laser-induced magnetism*

Inducing magnetism in nonmagnetic materials by means of the controlled helicity of laser fields is currently unraveling new paths for all-optical magnetic switching. The resonant interaction between an electromagnetic field and the conduction electrons in a metal, giving rise to collective oscillations, is one of the key controlling parameters of the underlying mechanism. A typical example of this interaction is the localized surface plasmon (LSP) in a gold nanoparticle excited by a short laser pulse, which corresponds to the coherent oscillations of the electron cloud, leading to a strong local enhancement of the electric field.[1]

The plasmonic properties can be used to enhance and tailor the magnetic properties of matter at nanoscale thanks to the material-specific magneto-optical response. This has already been applied to all-optical magnetic switching in ferri- or ferromagnetic materials and graphene.[2−10] Surface plasmon polaritons were used for improving light-assisted magnetic switching mechanisms,[9,10] giving rise to the field of magneto-plasmonics. It has been shown that one of the possible pathways to enable fast all-optical switching is the inverse Faraday effect (IFE),[2,4,5,7] which corresponds to a transfer of angular momentum from a circularly polarized laser field to the electronic system, leading to the creation of a static magnetization.[11] For instance, the Faraday rotation in gold-coated maghemite nanoparticles can be increased thanks to the plasmonic properties of gold.[12] Similarly, the magneto-optical response of nickel nanodisks can be adjusted by controlling the phase of the localized surface plasmons.[13] In this context, very recently, light-induced magnetism in plasmonic gold nanoparticles has also been reported.[14]

The inverse Faraday effect has been investigated using different theoretical approaches.[15−18] This effect was also studied for different bulk materials using density functional theory (DFT),[19] and the effect of spin−orbit coupling was also recently explored.[17] The plasmonic properties of the inverse Faraday effect in metal nanoparticles were also investigated by several groups.[20,21] In a recent work,[22] some of the authors of the present study used a quantum hydrodynamic (QHD) model[23−25] to describe the interaction between the surface plasmons in gold nanoparticles and circularly polarized light. It was shown that, under the action of a circularly polarized laser field at the LSP frequency, the gold nanoparticles can acquire a static magnetic moment whose direction is reversed when changing the light polarization. The model stressed the

Received: March 23, 2020
Published: July 20, 2020

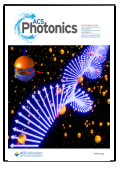

https://dx.doi.org/10.1021/acsphotonics.0c00462
ACS Photonics 2020, 7, 2429−2439

importance of the finite size of the electronic system: LSP generates electronic currents localized on the surface of the nanoparticle, which in turn create a quasi-static orbital magnetic moment. However, in this model, the electrons are treated as a charged fluid[23,25−27] and lack the orbital resolution of a fully quantum-mechanical description of an electronic system. Therefore, although the QHD model and previous theoretical approaches describe the magneto-optical responses in nanoparticles reasonably well, a thorough understanding of the chiro-optical dynamics of the generation of an orbital magnetic moment in metallic nanoparticles is still missing from a fully quantum many-body perspective.

In the present work, we investigate the orbital magnetism using a quantum mechanical method for many-body systems, namely, the real-time approach of the time-dependent density-functional theory (RT-TDDFT). Calculations are performed for jellium spherical nanoparticles (size $\lesssim$ 6 nm) containing different numbers of electrons in order to study the effect of size on the generated orbital angular momentum. The generation of an orbital angular momentum and the associated magnetic moment through the IFE is fully confirmed and its magnitude is consistent with results based on the QHD[22] model. We discuss the effects of the energy and polarization angle of the incident laser field on the magnetic moment generation. Finally, we study the effect of chemical species (K, Na, and Au) by comparing results for different Wigner-Seitz radii for two different cases: nanoparticles having the same number of electrons and nanoparticles having the same jellium radius.

The present study confirms that orbital magnetism can be successfully triggered through the IFE by irradiating non-magnetic nanoparticles with circularly polarized light. The resulting magnetic moment is significant (about 0.04 μ_B per electron in the best case for K) and robust over a wide range of parameters, including atomic species, laser intensity, and size of the nanoparticle. The crucial point is that the material should support a strong plasmonic response at the driving laser frequency. The generated magnetic moment could be tailored to trigger ultrafast all-optical switching in nanometric systems such as core/shell nanoparticles.[28,29]

Theoretical Background. The real-time approach of the time-dependent density-functional theory (RT-TDDFT) is used to study the optical response in metallic systems. The evolution of the many-electron system under an external perturbation is obtained from the solution of the time-dependent Kohn−Sham equations under the action of an effective time-dependent potential, which is a functional of the time-dependent electron density $n(\mathbf{r}, t)$. The effective potential contains both the Hartree and the exchange-correlation contributions. The latter is not known exactly and, in practice, requires to be approximated. In this work, we have employed the adiabatic local-density approximation (ALDA), which suffices to describe energy absorption in metallic jellium systems, where collective excitations dominate the spectrum.

The ground state electron density of the jellium system is calculated in static DFT. The absorption spectrum is obtained in RT-TDDFT using the time-propagation formalism of Yabana and Bertsch.[30,31] The system is excited by an electric field with strength K_0, having a temporal form of a dirac-delta function, and linearly polarized along a given direction, say z,

$$\delta E(\mathbf{r}, t) = K_0 \delta(t) \mathbf{e}_z \tag{1}$$

From the time-dependent induced density $\delta n(\mathbf{r}, t)$ corresponding to this excitation, the frequency-dependent absorption cross-section is obtained through Fourier transformation as

$$\sigma_{abs}(\omega) = -\frac{4\pi\omega}{cK_0}\mathrm{Im}\int_0^\infty \mathrm{d}t\ e^{i\omega t}\int_V \mathrm{d}\mathbf{r}\ z\ \delta n(\mathbf{r}, t) \tag{2}$$

where c is the speed of light and V denotes the volume of integration. For a spherically symmetric jellium system, eq 2 gives the total absorption spectrum. The strength K_0 in eq 1 is usually chosen such that the perturbation remains within the linear response regime.

In the present work, we use a homogeneous circularly (or, more generally, elliptically) polarized field to trigger the generation of an orbital angular momentum in the nanoparticle. The homogeneous electric field can be written as $\mathbf{E} = (E_x, E_y, 0)$, where

$$E_x(t) = \begin{cases} E_0\ \cos(\omega t)\sin\left(\frac{\pi t}{T}\right), & 0 \le t \le T \\ 0, & \text{otherwise} \end{cases} \tag{3}$$

$$E_y(t) = \begin{cases} E_0\ \cos(\omega t - \phi)\sin\left(\frac{\pi t}{T}\right), & 0 \le t \le T \\ 0, & \text{otherwise} \end{cases} \tag{4}$$

Here, ϕ is the polarization angle ($\phi = \pm 90°$ for left or right circularly polarized light). The second sinusoidal term in eqs 3 and 4 constitutes the temporal envelope of the pulse, which has a duration equal to T. As shown in Figure S2 of the Supporting Information, a Gaussian functional form could also be chosen for the temporal envelope, without changing significantly the results.

The time-dependent current density $\mathbf{j}(\mathbf{r}, t)$ is obtained in the length gauge from the time-dependent Kohn−Sham wave functions $\varphi_k(\mathbf{r}, t)$ as

$$\mathbf{j}(\mathbf{r}, t) = \frac{-ie\hbar}{2m_e}\sum_{k=1}^{N} \varphi_k^*(\mathbf{r}, t)\nabla\varphi_k(\mathbf{r}, t) - \varphi_k(\mathbf{r}, t)\nabla\varphi_k^*(\mathbf{r}, t) \tag{5}$$

where N is the total number of Kohn−Sham states, m_e and e are, respectively, the mass and charge of the electron, and $\hbar$ is Planck's constant. The total orbital magnetic moment generated in the system is then obtained from the time-dependent current density as

$$\mathbf{M}(t) = \frac{1}{2}\int_V \mathrm{d}\mathbf{r}\ \mathbf{r} \times \mathbf{j}(\mathbf{r}, t) \tag{6}$$

We will also use, as a diagnostic tool, the dipole moment, which is defined as

$$\mathbf{p}(t) = \int_V \mathrm{d}\mathbf{r}\ \mathbf{r}\ \delta n(\mathbf{r}, t) \tag{7}$$

where $\delta n(\mathbf{r}, t)$ is the time-dependent induced density corresponding to the excitation by the laser field.

Systems and Simulation Details. We study jellium spheres with valence electron densities corresponding to three different chemical species, K, Na, and Au, with values of the Wigner-Seitz radius being r_s = 2.572, 2.083, and 1.593 Å, respectively. The radius of the jellium sphere is related to the total number of electrons N_e through the expression $R = N_e^{1/3} r_s$. For Au, we have considered only the s electrons and no

https://dx.doi.org/10.1021/acsphotonics.0c00462
ACS Photonics 2020, 7, 2429−2439

polarizable jellium background is used in the model to mimic the dynamical screening by the d electrons.[32,33] All the calculations are performed using the real-space code octopus.[34] The calculation domain is taken to be a sphere centered at the center of the nanoparticle. The radius of the calculation domain is chosen to be 5.0 Å; larger than the radius of the jellium nanoparticle. The real-space grid spacing was set to 0.5 Å for simple metals (K and Na) and 0.25 Å for the noble metal. For the calculation of the ground-state electron density, a stopping criterion of 10^{-7} Å^{-3} for the relative electron density is chosen for the convergence of the self-consistent loop. For the time evolution, a time-step of 0.00658 fs (≈0.01 $\hbar$/eV ≈ 0.272 $\hbar$/Hartree) is used for all the systems. The absorption spectra are obtained from a total evolution time of ≈25 fs.

In the calculations using a circularly polarized electric field, the amplitude of the field was set to E_0 = 0.01 V/Å = 10^8 V/m, corresponding to a peak laser intensity (I_0) of 1.327 × 10^9 W/cm^2. This choice is made so that the perturbation remains weak enough for the response to be within the linear regime and for avoiding photo ionization. The duration of the laser pulse was set to T ≈ 13.16 fs for all the calculations. We have studied the optical response for different values of the polarization angle, changing the polarization gradually from circular (ϕ = 90°) to elliptical (ϕ = 60° and 30°) and finally to linear (ϕ = 0°) polarization. The response of the system is calculated for a time duration equal to twice the duration of the laser pulse.

Magnetic Moment Generation. In this section, we describe the effect of the energy and the polarization of the incident laser field on the generation of angular momentum and present the spatiotemporal dynamics of the electron density and current density at the plasmon energy. The absorption spectra calculated using the adiabatic local-density approximation (TD-ALDA) for potassium clusters of different sizes are shown in Figure 1. They show the well-known red

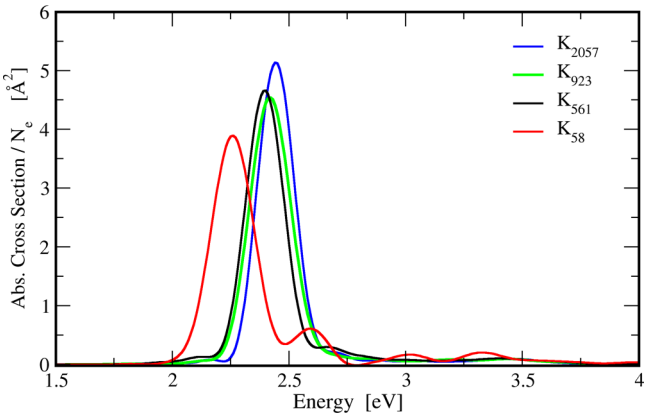

Figure 1. Absorption spectra for potassium jellium clusters of different sizes: K_{58}, K_{561}, K_{923}, and K_{2057}. The spectra are normalized to the total number of electrons contained in the system.

shift[35,36] of the LSP peak in a simple metal as the size decreases. This red shift is attributed to the spill-out[37] of the ground state electron density, which becomes more and more significant with decreasing jellium radius, see Figure S1 in the Supporting Information. Moreover, we note that other spectral features than the plasmonic peak appear, due to the fragmentation of the collective excitation in the spectrum of the smallest system considered here (K_{58}).

The absorption spectrum of jellium K_{561} cluster displays a single prominent plasmon peak at 2.39 eV with a full-width at half-maximum of ≈0.18 eV, as shown in Figure 1. In order to study the effect of the laser frequency on the generation of a magnetic moment, we calculated the response of this system for quasi-monochomatic circularly polarized pulses with frequencies 2.39 eV (at the plasmon resonance) and 1.55 eV (off-resonance). The results of the TDDFT simulations are presented in Figure 2, for the on-resonance (right panels) and off-resonance (left panels) cases. This figure shows several features of the laser excitation (laser electric field) and the electronic response of the system (dipole moment, absorbed energy, magnetic moment). The differences between the resonant and off-resonant response of the system are clearly captured in the magnitudes of both the dipole moment (panels (b) and (f)) and the absorbed energy (panels (c) and (g)).

As it can be seen in panels (d) and (h) of Figure 2, the generated magnetic moment (M_z) is 2 orders of magnitude larger at resonance as compared to the off-resonance case. The x and y components of the magnetic moment (Figure 2h) remain negligibly small, as they should be, both during and after the laser excitation. In contrast, M_z increases in time and closely follows the time dependence of the energy absorbed by the system. After the laser is turned-off, both the total energy and M_z reach saturation values, as they are conserved in the simulation. These results are in line with earlier findings using a QHD approach,[22] thus, confirming that the observed magnetic moment generation is indeed a resonant plasmonic effect. At the end of the laser pulse, the total energy given to the system remains constant, see Figure 2g. The energy does not decay as there is no decay channel (radiation losses, etc.) present in the simulations. However, Landau damping, which accounts for the phase mixing between the electronic states, is taken into account and can be observed in the time-dependent dipole moments, which slowly decay in time, see Figure 2f.

In Figure 3, we present the time dependence of the normalized dipole moment (top panel) and the normalized z component of the magnetic moment $M_z(t)$ (bottom panel) generated in a K_{561} jellium sphere, for different values of the peak amplitude E_0 of the circularly polarized laser field. The dipole moments are divided by the corresponding E_0, whereas $M_z(t)$ is divided by E_0^2 (this is because the IFE is proportional to the intensity of the laser, hence, to the square of the electric field). The figure shows that, below E_0 ≈ 0.01 V/Å, the corresponding normalized dipole moments do not differ from each other, signaling that in this range the electron response is linear. The transition to the nonlinear response regime takes place between E_0 = 0.01 V/Å and E_0 = 0.1 V/Å; as for E_0 = 0.1 V/Å, the amplitude of both the normalized dipole and the normalized magnetic moment is no longer proportional to the excitation. For even larger amplitudes (E_0 = 1 V/Å, not shown in the figure), the systems are very strongly perturbed and go into the ionization regime. Figure 3 ensures that, by choosing E_0 = 0.01 V/Å, we remain indeed within the linear response regime. Incidentally, it also confirms that the induced magnetization is due to the IFE in the linear response regime, as it follows the same scaling with the field intensity as that of IFE.

The polarization of the laser field is defined by the phase difference ϕ between the x and y components of the electric field, see eqs 3 and 4. In order to study the effect of the polarization, we have calculated the magnetic moment generation in K_{561} using different values of ϕ. The time-

https://dx.doi.org/10.1021/acsphotonics.0c00462
ACS Photonics 2020, 7, 2429−2439

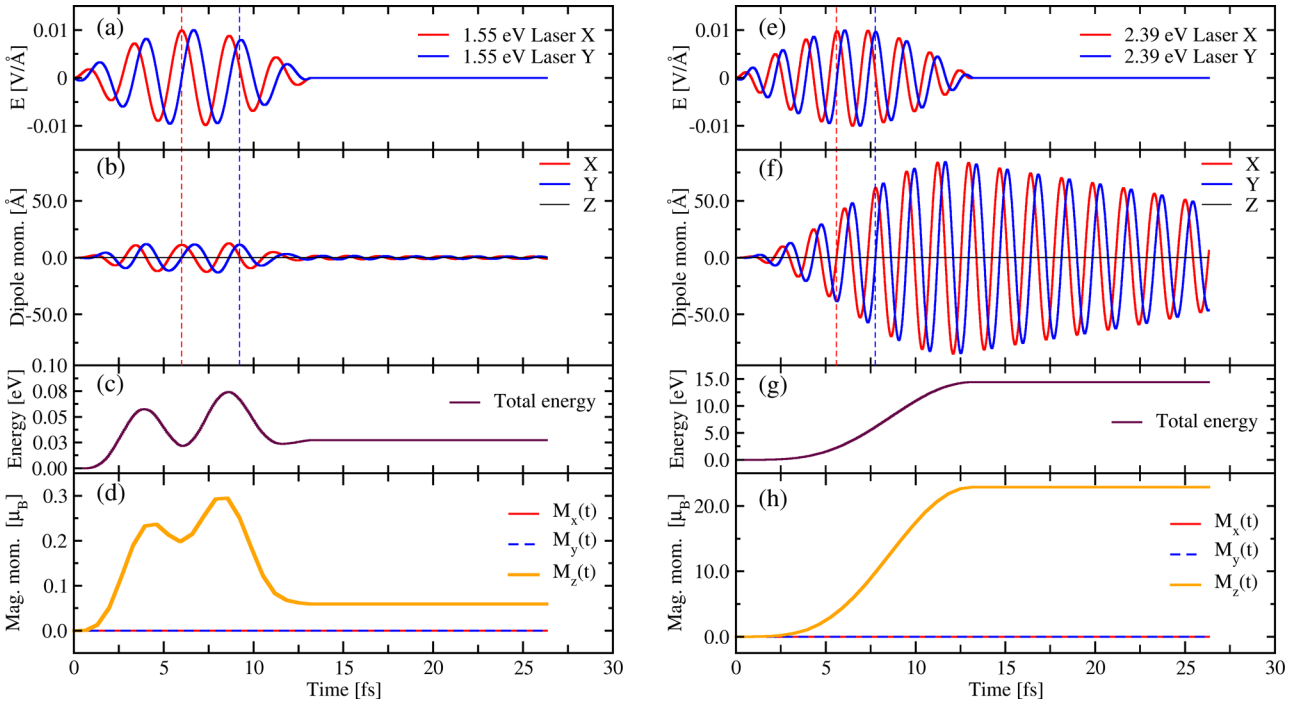

Figure 2. Quasi-monochromatic circularly polarized laser excitation of a jellium K_{561} cluster. Panels on the left and right columns represent respectively a nonresonant (1.55 eV) and a resonant (2.39 eV) excitation. From top to bottom, the panels (a) and (e) show the time dependence of the x (red) and y (blue) components of the laser electric field in V/Å; panels (b) and (f) show the three components of the dipole moment in Å; panels (c) and (g) show the total energy absorbed by the electronic system in eV; and panels (d) and (h) show the three components of the magnetic moment, in units of the Bohr magneton μ_B.

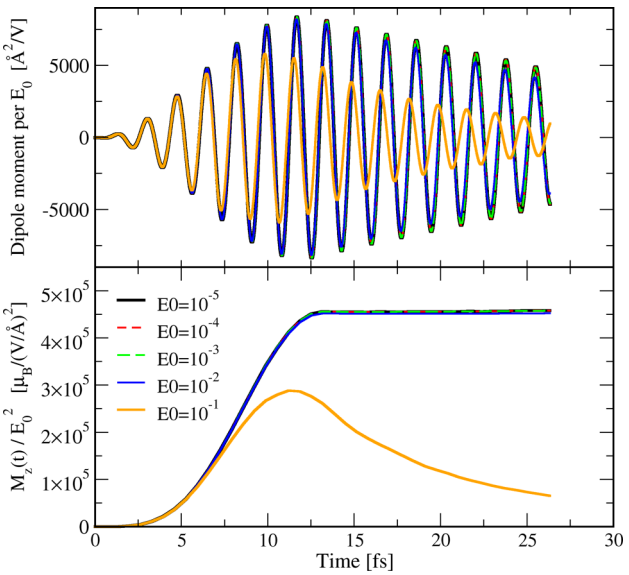

Figure 3. Top panel: Time-dependent dipole moments (y components) divided by the peak amplitude E_0 of the laser field, for different values of E_0 ranging from 10^{-5} to 10^{-1} V/Å. Bottom panel: Time evolution of the z component of the generated magnetic moment M_z, divided by E_0^2 (in units of μ_B Å^2/V^2). The simulations were performed for the K_{561} spherical nanoparticle.

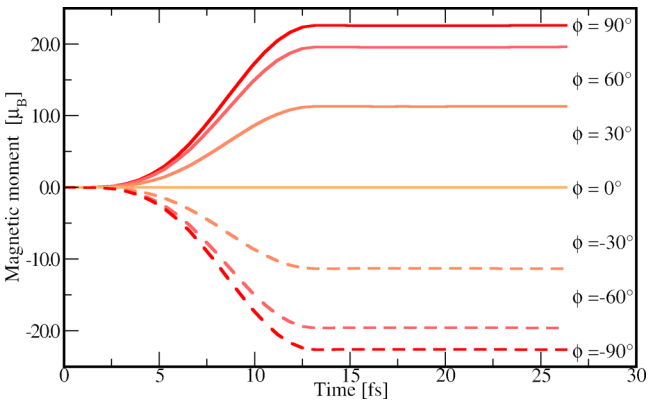

Figure 4. Generated magnetic moment $M_z(t)$ (in units of μ_B) in a jellium K_{561} cluster for different polarizations of the perturbing laser field: circular $|\phi| = 90°$, elliptical $|\phi| = 60°$, 30°, linear $|\phi| = 0°$ polarizations.

dependence of the z component of the generated magnetic moment for different values of ϕ is shown in Figure 4. M_z is maximum for a circularly polarized laser pulse ($|\phi| = 90°$), vanishes for linear polarization ($|\phi| = 0°$), and takes on intermediate values for elliptically polarized fields. Changing from left to right polarized fields induces a reversal of the magnetic moment (change in the sign of M_z). Thus, by changing the polarization phase ϕ, one can tune the magnetic moment at saturation in a wide range of values in both directions.

Induced Density. As shown in Figure 2, the generation of a magnetic moment in a K_{561} jellium sphere is strongly favored at the LSP frequency. In order to better understand the influence of the LSP on the magnetic moment generation, we have studied the induced time-dependent density, from the corresponding TDDFT simulation. The induced density is defined as

$$\delta n(\mathbf{r}, t) = n(\mathbf{r}, t) - n_{GS}(\mathbf{r}) \quad (8)$$

https://dx.doi.org/10.1021/acsphotonics.0c00462
ACS Photonics 2020, 7, 2429−2439

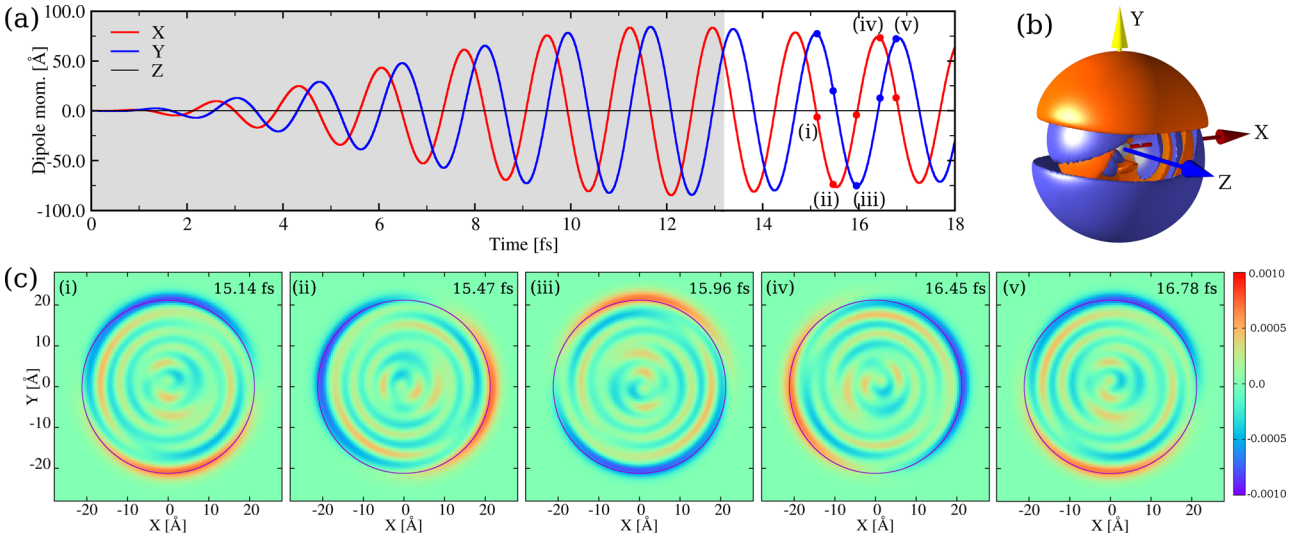

Figure 5. Response of a K_{561} spherical nanoparticle excited by circularly polarized light at the plasmon frequency (2.39 eV). (a) Time evolution of the three components of the dipole moment. The shaded gray area represents the duration of the laser pulse. (b) Three-dimensional iso-surface of the induced density at time t = 15.96 fs. (c) Snapshots of the induced electron density at five different times corresponding to the red and blue dots on the dipole moment curves in panel (a). The solid circle represents the jellium boundary and the induced density is shown as a color map, where the colors correspond to values of the color bar (on the right) in units of electrons per Å^3.

where n_{GS} is the ground-state electron density. The result is presented in Figure 5. The contents of panel (a) of Figure 5 is the same as in panel (f) of Figure 2. It shows the time-dependence of the dipole moment in K_{561} due to the excitation by right-circularly polarized light at the LSP frequency. The shaded gray area corresponds to the duration of the laser pulse. In Figure 5b, we show an isosurface of the induced density $\delta n(\mathbf{r}, t)$ at time t = 15.96 fs, that is, after the laser is switched off. The induced density shows accumulation of opposite charges (represented by the two different colors) at the surface of the jellium sphere along the y-direction. This confirms that the LSP mode is dipolar and also that, at time t = 15.96 fs, the y-component of the dipole moment reaches a maximum, as indicated by the blue dot (iii) in panel (a). We note that, at this instant, the x-component of the dipole moment is close to zero. However, the induced density also shows other contributions from the interior of the sphere, which are concentric and not fully symmetric along the y-direction.

In order to better understand the time-dependent evolution of the electron density, we have taken snapshots of the induced density for five different instants, indicated by the red and blue dots, respectively, on the x- and y-components of the dipole moment in Figure 5a. All five snapshots at times (i) 15.14 fs, (ii) 15.47 fs, (iii) 15.96 fs, (iv) 16.45 fs, and (v) 16.78 fs together represent a full period of the circular rotation of the total dipole moment and, hence, of the induced electron density of the system after the laser is switched off. The snapshots of these induced densities are shown in five different panels in Figure 5c, which represent the induced electron density in the (x, y) plane passing through the center of the jellium sphere and parallel to the plane of polarization (z = 0). These snapshots confirm that, at the LSP frequency, the principal contribution responsible for the circular motion of the induced density lies at the surface of the cluster. As we move from the surface to the center of the cluster, we notice that dipolar contributions of a smaller magnitude than at the surface form concentric shells of different radii. These contributions correspond to those captured at the interior of the system in the isosurface representation of the induced density in panel (b). The origin of these contributions is fully quantum mechanical and can be traced back to the Friedel-like radially oscillating nature of the ground-state electron density[38] (cf. Figure S1 of the Supporting Information). A careful observation reveals that, although these shells are undergoing the same circular motion as the surface contribution, there exists a lag of phase between them. An animation presenting the time-dependent circular motion of the induced density is given in Figure S3 of the Supporting Information. Figure 5 shows that, when the cluster is excited by a circularly polarized wave at the LSP frequency, the surface of the system plays the leading role in the circular motion of the induced electron density and hence also in the generation of the magnetic moment.

Current Density. The current density directly concerns the generation of the magnetic moment through eq 6. Consequently, we have studied the spatial behavior of $\mathbf{j}(\mathbf{r}, t)$ after switching off the laser ($t > T$) in K_{561}. Figure 6 shows the spatial distribution of the current density $\mathbf{j}(x, y, 0)$ in the z = 0 plane, which is parallel to the polarization plane of the driving field. The current density is shown at every third grid point (shown in red dots) of the real-space grid on which it was computed (using the octopus code). The top panel of Figure 6 shows $\mathbf{j}(x, y, 0)$ at the time 15.96 fs for which the induced densities are shown in Figure 5b and also in the middle panel of Figure 5c. At a given instant of time after the laser is switched off, the current density within the cluster is not directed toward a preferred direction. The origin of these fluctuations of the instantaneous current is quantum-mechanical and is related to the size-confinement effects that give rise to Friedel-like oscillations of the electron density. This effect was not captured in the earlier QHD model. An animation that displays the time-dependent current corresponding to the full period of the dipole oscillation between instants (i) and (v) of Figure 5a is given in Figure S3 of the Supporting Information.

https://dx.doi.org/10.1021/acsphotonics.0c00462
ACS Photonics 2020, 7, 2429−2439

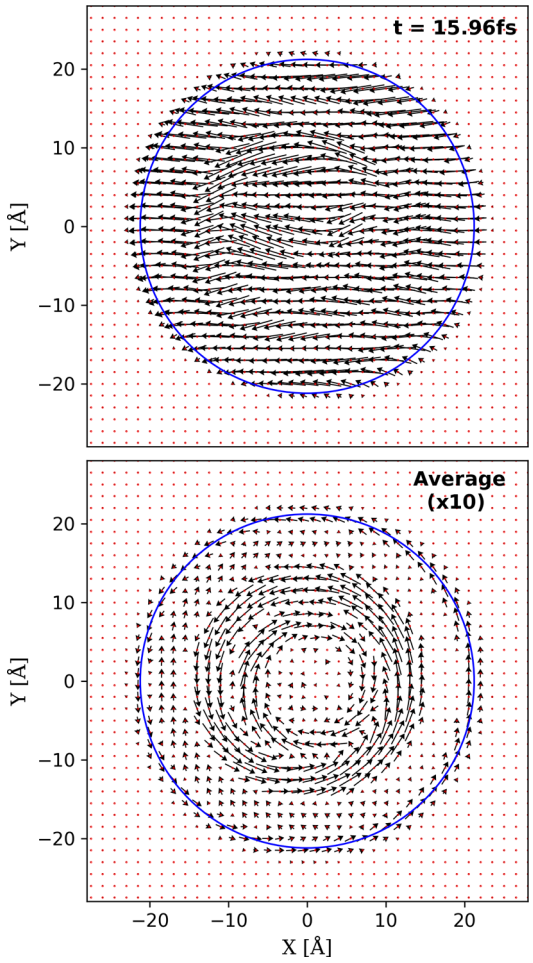

Figure 6. Blue circles shows the jellium boundary of K_{561}. The red dots are grid points. Top panel: current density $\mathbf{j}(x, y, 0)$ at $z = 0$ at time 15.96 fs. The arrows' length and direction, respectively, correspond to the magnitude and the direction of the current. Bottom panel: $\mathbf{j}(x, y, 0)$ averaged over one period of oscillation of the dipole moment and multiplied by 10.

The bottom panel of Figure 6 shows the current density for the same $z = 0$ plane as in the top panel, but averaged over one period of oscillation of the dipole moment. In order to produce a magnetic moment, the current must form a loop. In the case of a metal cluster, this is achieved by a full rotation of its free electron density. Therefore, the spatial distribution of the average current density in Figure 6 shows the region of space where current loops are formed to generate the saturated magnetic moment in the cluster. As expected at the LSP frequency, there is a nonvanishing current at the surface of the cluster. However, at the interior of the cluster there are also two different concentric loops of current: one of them is rotating in the sense of the current at the surface and the other is rotating in the opposite sense. From the figure, it is qualitatively clear that the resultant of the contributions of all these different loops creates a magnetic moment along the z direction. This result, along with the observations on the induced density in Figure 5, confirms that, although the surface takes a leading role in the generation of the magnetic moment through IFE, contributions from the core of the cluster are of comparable importance.

Effect of Cluster Size and Chemical Species. In order to study the effect of size and chemical species on the generation of angular momentum, we have performed RT-TDDFT calculations for jellium clusters of K, Na, and Au having different numbers of electrons. Here the different chemical species differ from each other only by their respective values of the Wigner-Seitz radius r_s. The LSP resonant frequencies for these systems are obtained from the absorption spectra calculated in TD-ALDA.

Effect of Size for the Same Chemical Species. Four different jellium spheres of potassium containing, respectively, N_e = 58, 561, 923, and 2057 electrons are considered. These values of N_e have been chosen so that the jellium systems contain the same number of electrons as the number of atoms in icosahedral clusters (except for K_{58}). The jellium radii and the TD-ALDA calculated LSP frequencies are listed in Table 1. The absorption spectra were shown in Figure 1.

Table 1. Properties of the Various Jellium Clusters

r_s (Å)	system	R (Å)	ω_p (eV)
2.572	K_{58}	9.955	2.26
	K_{561}	21.211	2.39
	K_{923}	25.040	2.42
	K_{2057}	32.707	2.44
2.083	Na_{58}	8.06	2.89
	Na_{106}	9.86	3.10
1.593	Au_{58}	6.165	4.01
	Au_{254}	10.08	4.82

The systems are excited by circularly polarized electric fields at their respective plasmon frequencies. The results are displayed in Figure 7. For all cases, the evolution of the M_z component of the magnetic moment displays an initial growth, followed by saturation when the laser is switched off (left panel). The value reached by M_z at saturation scales linearly with the number of electrons N_e in the system as shown in the right panel of Figure 7. This indicates that the per-electron magnetic moment generated through IFE remains constant for clusters with a diameter of up to ∼6.5 nm, such as those considered here (see Table 1).

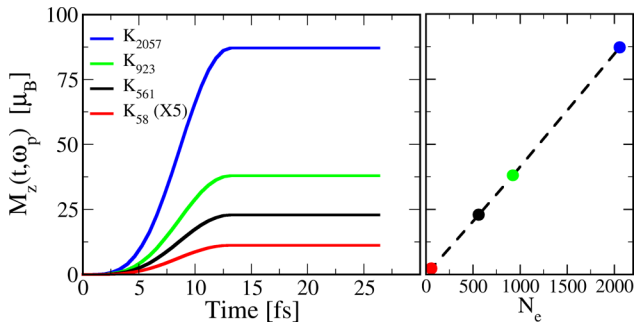

Figure 7. Left panel: Time dependence of the z-component of the generated magnetic moment (in units of μ_B) for different potassium clusters. For K_{58}, the values are multiplied by a factor 5 in order to make them visible in the same scale. Right panel: saturated z-components of the generated magnetic moment vs the number of electrons.

Effect of Chemical Species for the Same Radius. In order to study the effect of the chemical species on clusters of the same size, we consider jellium spheres of sodium (Na_{106}) and gold (Au_{254}), which have almost the same jellium radius as that of K_{58}. The absorption spectra calculated in TD-ALDA for

https://dx.doi.org/10.1021/acsphotonics.0c00462
ACS Photonics 2020, 7, 2429−2439

these three systems are shown in Figure S4 of the Supporting Information. The Wigner-Seitz radii r_s, jellium radii, and the LSP frequencies are summarized in Table 1. The systems are then excited by circularly polarized light at their respective plasmon frequencies. The results of the simulation are shown in Figure 8.

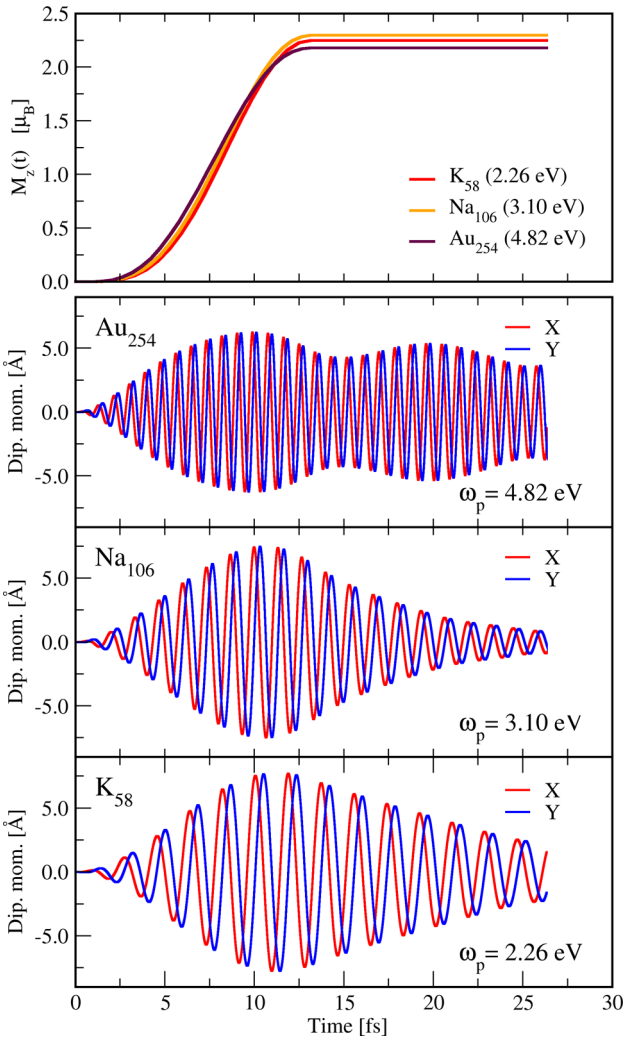

Figure 8. Top panel: Magnetic moment $M_z(t)$ in K_{58} (red), Na_{106} (orange), and Au_{254} (brown) clusters generated through excitation by circularly polarized light at respective LSP frequencies. The three jellium systems have almost the same radius (see Table 1). Lower panels: Time dependence of the x (red) and y (blue) components of the induced dipole moment for each system.

The topmost panel shows $M_z(t)$ for the three systems. Although they are excited at different respective LSP frequencies, the generated magnetic moments are very similar to each other. On the contrary, the induced dipole moments are rather different. This can be attributed to the fact that Landau damping is different for different chemical species (cf. Figure S4 in the Supporting Information). Nevertheless, the dipole moments display similar maximum amplitudes for all cases (≈5.5 Å).

The pulse duration of the lasers used for the three different systems is the same. Therefore, as the frequencies are different, the number of oscillations of the electric field within the pulse duration is not the same. Hence, during the laser excitation, the three clusters did not absorb the same amount of energy (as listed in Table 2). The total energy absorbed by the three

Table 2. Total Energy Absorbed by Various Types of Clusters

cluster	ω_p (eV)	E_{tot} (eV)
K_{58}	2.26	1.335
Na_{58}	2.89	0.94442
Na_{106}	3.10	1.8756
Au_{58}	4.01	0.75508
Au_{254}	4.82	2.7425

clusters as a function of time is shown in Figure S4 of the Supporting Information. In order to better understand the effect of the chemical species, the generated magnetic moment normalized to the total absorbed energy $M_z(t)/E_{tot}$ is shown in Figure 9, left panel. This quantity is the maximum for K_{58} and

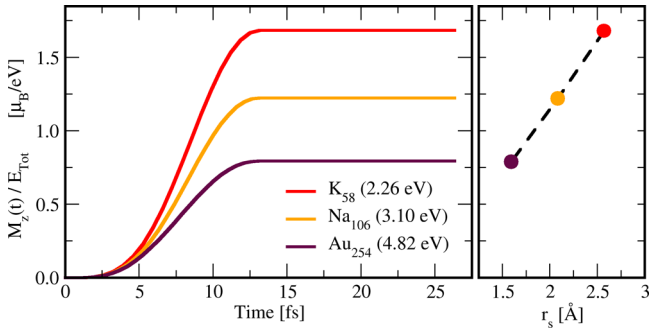

Figure 9. Time evolution of the z component of the generated magnetic moment $M_z(t)$, divided by the total absorbed energy, for K_{58} (brown), Na_{106} (red), and Au_{254} (orange).

minimum for Au_{254} and appears to be directly proportional to the Wigner-Seitz radius r_s of each species, as shown in Figure 9, right panel.

Effect of Chemical Species for the Same N_e. We consider jellium clusters of potassium, sodium, and gold, all having 58 electrons (their characteristics are summarized in Table 1) and excited by circularly polarized laser at their respective LSP frequencies. The TD-ALDA absorption spectra of K_{58}, Na_{58}, and Au_{58} are provided in Figure S5 of the Supporting Information. Unlike in Figure 8 (clusters of same size, but different N_e), here the three systems with the same N_e do not display a similar M_z at saturation (cf. Figure 10). The dipole moments are also rather very different from each other in this case.

The total energy pumped by the laser pulse into these 58-electron jellium spheres is given in Table 2 and in Figure S5 of the Supporting Information. In Figure 11, we plot the magnetic moment M_z normalized to such energy, which shows that M_z/E_{tot} is the maximum for K_{58} and the minimum for Au_{58}. Thus, also in this case, M_z/E_{tot} appears to be proportional to the Wigner-Seitz radius r_s of the material.

Classical Model. A simple illustration of our findings can be obtained by making use of a classical Drude-like model for the linear response of electrons in the nanoparticle. Considering electric field propagation in the z-direction, the electronic dipoles $d_x(t)$ and $d_y(t)$ in the transverse plane obey the linearized equations of motion:

https://dx.doi.org/10.1021/acsphotonics.0c00462
ACS Photonics 2020, 7, 2429−2439

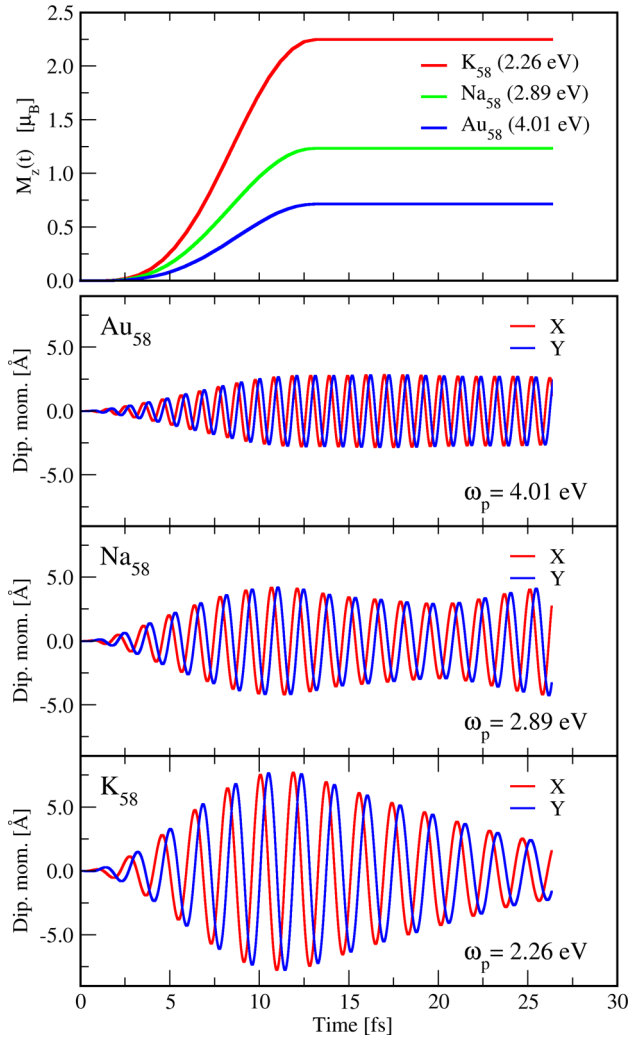

Figure 10. Top panel: $M_z(t)$ for K_{58} (red), Na_{58} (green), and Au_{58}(blue) clusters due to excitation by circularly polarized light at respective LSP frequencies (see Table 1). The three jellium systems have the same number of electrons. Bottom panel: time dependence of the x (red) and y (blue) component of the corresponding induced dipole moments.

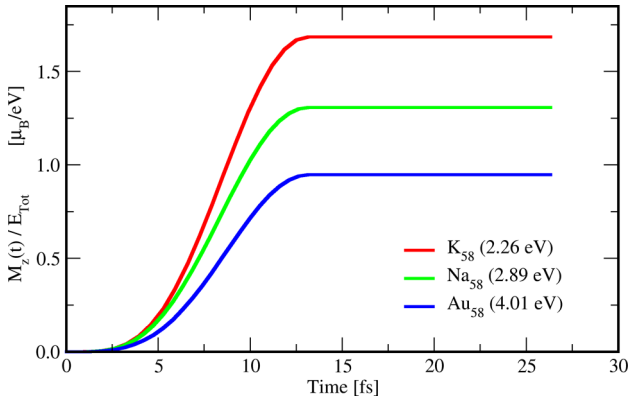

Figure 11. Time dependence of the z-component of the generated magnetic moment per unit energy absorbed by the system for K_{58} (red), Na_{58} (green), and Au_{58} (blue) clusters.

$$\ddot{d}_x = -\omega_{\mathrm{Mie}}^2 d_x - \gamma \dot{d}_x + \frac{e}{m_e} E_x(t) \tag{9}$$

$$\ddot{d}_y = -\omega_{\mathrm{Mie}}^2 d_y - \gamma \dot{d}_y + \frac{e}{m_e} E_y(t) \tag{10}$$

Here, e and m_e are, respectively, the charge and mass of an electron, $E_x(t)$ and $E_y(t)$ are, respectively, the x and y component of the electric field, ω_{Mie} is the Mie frequency, which is a good approximation of the surface plasmon frequency for relatively large nanoparticles, and γ is a phenomenological damping rate that incorporates the effect of all incoherent interactions between the collective electron modes (Landau damping) and between the electrons and the environment. The dipoles are excited by an elliptically polarized monochromatic laser pulse, with frequency ω_L and phase shift ϕ_L:

$$E_x(t) = E_0 \cos(\omega_L t), \quad E_y(t) = E_0 \cos(\omega_L t + \phi_L) \tag{11}$$

For simplicity, we have neglected the envelope of the laser pulse.

We consider solutions of eqs 9 and 10 in the stationary regime, where the dipoles are assumed to oscillate at a single frequency, equal to the laser frequency ω_L. In this case, the general solutions for the two dipole modes can be written as

$$d_x(t) = d_0 \cos(\omega_L t + \varphi) \tag{12}$$

$$d_y(t) = d_0 \cos(\omega_L t + \varphi') \tag{13}$$

where d_0 denotes the amplitude of the dipole modes. Injecting eqs 12 and 13 into eqs 9 and 10, we get

$$\tan(\varphi) = \frac{\gamma \omega_L}{\omega_L^2 - \omega_{\mathrm{Mie}}^2} \tag{14}$$

and $\varphi' = \varphi + \phi_L$, that is, the phase shift between the two dipoles is the same as the one between the two corresponding components of the electric field. We also obtain the relation between the amplitude of the dipole modes and the amplitude of the electric field:

$$d_0 = \frac{eE_0/m_e}{[(\omega_L^2 - \omega_{\mathrm{Mie}}^2)^2 + \gamma^2 \omega_L^2]^{1/2}} \tag{15}$$

As expected, eq 15 corroborates that the dipoles are strongly excited at the surface plasmon resonance, where $\omega_L = \omega_{\mathrm{Mie}}$.

Considering a homogeneous electron density for a spherical metallic nanoparticle, the magnetic moment associated with the displacement of the center of mass of the electron gas can be written as[15,22]

$$\mathbf{M} = \frac{1}{2}\int \boldsymbol{r} \times \boldsymbol{j}\, \mathrm{d}\boldsymbol{r} = -\frac{Ne}{2}\boldsymbol{d}(t) \times \dot{\boldsymbol{d}}(t) \tag{16}$$

where N is the total number of electrons in the nanoparticle. Injecting the expressions of the two dipoles (eqs 12 and 13), together with eq 15, into eq 16, we obtain

$$M_z = \frac{N}{2}\frac{e^3}{m_e^2}\frac{\omega_L E_0^2 \sin(\phi_L)}{(\omega_L^2 - \omega_{\mathrm{Mie}}^2)^2 + \gamma^2 \omega_L^2} \tag{17}$$

The above expression corresponds to the classical inverse Faraday effect in a nanoparticle containing N delocalized electrons. Indeed, the magnetization is proportional to the square of the electric field, vanishes for linearly polarized light ($\phi_L = 0$) and is maximum for circularly polarized light ($\phi_L = \pm\pi/2$). For small damping γ, the generated magnetic moment can reach very high values if the laser pulse is tuned at the surface plasmon frequency ($\omega_L = \omega_{\mathrm{Mie}}$). This simple result

https://dx.doi.org/10.1021/acsphotonics.0c00462
ACS Photonics 2020, 7, 2429−2439

demonstrates that the magnetic moment generation is indeed due to a plasmonic resonance.

Further, one can also show that the current density contribution relevant for the magnetic moment generation is localized on the nanoparticle surface. Following ref 39, the electron density can be written as

$$n = \langle n \rangle + \delta n \tag{18}$$

where $\langle n \rangle$ is the time-averaged value of the density (which is constant or slowly varying in time) and δn represents the rapidly oscillating fluctuation driven by the external electric field. In a finite-size object, such as a metal nanoparticle, δn is localized on the surface. The same decomposition can be made on the electric current density: $\boldsymbol{j} = \langle \boldsymbol{j} \rangle + \delta \boldsymbol{j}$. As δn and $\delta \boldsymbol{j}$ vary with the oscillating external electric field, they vanish when averaged over a period of oscillation, that is,

$$\langle \delta n \rangle = \langle \delta \boldsymbol{j} \rangle = 0 \tag{19}$$

Making use of the fact that $\delta n \ll n$ (linear response) and separating the slow and fast terms in the continuity equation, we obtain that

$$\delta \boldsymbol{j} = e\langle n \rangle \delta \boldsymbol{u} \tag{20}$$

where $\delta \boldsymbol{u}$ is the fluctuating part of the velocity.

In the Drude approximation, $\delta \boldsymbol{j} = \sigma \boldsymbol{E}$ (note that the electric field $\boldsymbol{E}$ only has an oscillating component), where $\sigma = i\langle n \rangle e^2/(m\omega_L)$ is the electric conductivity. Inserting the Drude expression into eq 20, we get the fluctuating part of the velocity

$$\delta \boldsymbol{u} = \frac{\sigma}{e\langle n \rangle} \boldsymbol{E} \tag{21}$$

Finally, using the time-averaged continuity equation and assuming $\langle \boldsymbol{u} \rangle = 0$, the slowly varying part of the current becomes

$$\langle \boldsymbol{j} \rangle = e\langle \delta n \delta \boldsymbol{u} \rangle = \frac{ie^2}{m_e \omega_L} \langle \delta n \boldsymbol{E} \rangle \tag{22}$$

From eq 22 it is clear that the time-averaged current $\langle \boldsymbol{j} \rangle$ is localized on the surface of the nanoparticle, because it is proportional to the localized density fluctuation δn. By contrast, the fluctuating current $\delta \boldsymbol{j}$ depends on the equilibrium density $\langle n \rangle$ (cf. eq 20) and not on δn. Thus, it is not localized on the surface. Moreover, it vanishes when averaged over a full period of oscillation (cf. eq 19). These conclusions are in line with our earlier results obtained using a QHD model[22] and with the present simulations, as shown in Figure 6.

Our RT-TDDFT simulations provide strong proof that the laser-induced generation of the magnetization is a robust effect, which persists even when the fully quantum, self-consistent, and nonlinear many-electron dynamics is taken into account. In addition, in contrast to the intuitive classical approach sketched above, the RT-TDDFT simulations also explore the quantum-mechanical effects due to the finite size of the nanoparticle. The resulting confinement of the electron gas gives rise to Friedel-like oscillations in the electron density (Figure 5), yielding in turn the spatial fluctuations of the instantaneous current density observed in Figure 6. Consequently, concentric contributions with opposed directions of rotation appear in the current density averaged over one period of oscillation (bottom panel of Figure 6). These interior contributions are of purely quantum-mechanical origin and cannot be captured by simple classical models.

DISCUSSION

In the simulations presented in Figures 8 and 10, the induced dipole moment at LSP frequency decays differently for different chemical species and for different sizes of the clusters. As no decay channel other than the Landau damping is incorporated, the observed decay of the dipole moments in the presented results is necessarily due to this effect, and corresponds to the electronic dephasing, that is, a decay of the phase correlations between the electron−hole excitations that form the plasmon. It is worth mentioning that, although the dipole moments are observed here to decay exponentially, due to the absence of other decay channels they would revive again later in time. This revival of dipole oscillations forms beat-like features as can be seen for the cases of Au_{254} (cf. Figure 8) and Na_{58} (cf. Figure 10). All these results together confirm that, in systems belonging to the size range considered here (see Table 1), Landau damping is important. An exception may be Au_{58}, where the plasmon peak is most likely due to a single highly renormalized electron−hole excitation, which remains well separated from any other neighboring excitation in the spectrum (cf. Figure S5, Supporting Information), therefore, resulting in almost no damping.

However, Figures 8 and 10 also indicate that Landau damping does not affect the magnetic moment generated in those systems. It also does not affect the total energy of the system, as can be seen from Figure 2. This is an intriguing result, as it suggests that the lifetime of the magnetic moment may be much larger than a few tens of femtoseconds, which was the duration of the simulations presented here. The absence of decay for $M_z(t)$ is linked to the conservation of the total angular momentum for the highly symmetric systems considered here. For systems possessing fewer symmetries, it may no longer be true, but further studies are needed to clarify this important issue. Of course, other energy-dissipating mechanisms, not included here, may also be responsible for the decay of M_z in metal clusters.

Another important issue concerning the generated orbital magnetic moment is the effect of the chemical species. Figures 9 and 11 shows that the magnetic moment generated per unit energy absorbed, and at LSP frequency is maximum in K and minimum in Au. To this end, we emphasize that we define chemical species through their r_s values only. In our simplified description, the Au clusters do not have d electrons nor do they have a polarizable background that would mimic the effect of the d electrons on the delocalized electrons of the system. Using a proper description of strongly localized d electrons, the dynamical response in the Au systems would be screened by their presence, which might diminish the generation of the orbital magnetic moment observed here. We would also like to mention that, in our simulations, we did not consider the spin degrees of freedom that, in principle, can couple to the orbital magnetic moment. Depending on the species-specific spin−orbit coupling, the overall induced magnetic moment can thus be modified. However, in this work we focused solely on the orbital magnetic moment and discussed its generation and dynamics. Spin effects are left for further studies.

Finally, for Au clusters we have compared the per-atom magnetic moment at saturation normalized with respect to pulse duration and peak intensity (i.e., $M_z/(N_e T I_0)$ and considering one electron per atom for Au), with the recent experimental results of Cheng et al.[14] For Au_{254} and Au_{58}, we obtained, respectively, 4.91 and 7.06 in units of μ_B m^2 fs^{-1} W^{-1}

https://dx.doi.org/10.1021/acsphotonics.0c00462
ACS Photonics 2020, 7, 2429−2439

$\times 10^{-17}$, which should be compared to 2.82 obtained from the experimental results.[14] The comparison is shown in Table T1 of the Supporting Information. One of the reasons for getting higher values in calculations is that, unlike in the experiment,[14] the presented calculations do not take into account the effects of the chemical environment around the Au clusters in solution.

CONCLUSION

In this work, we have presented real-time TDDFT calculations for the optical response of jellium clusters excited by circularly polarized laser fields in the linear-response regime. We have considered the effects of different physical parameters, both pertaining to the laser (frequency, polarization, intensity) and to the clusters (size and chemical species).

We showed that irradiating small metal clusters with circularly polarized laser light induces an orbital magnetic moment M_z through the inverse Faraday effect. Similar to results obtained in an earlier study using a simpler QHD model,[22] we showed that orbital magnetic moment generation is a resonant effect and only occurs at or near the surface plasmon frequency of the cluster. In the linear-response regime, M_z scales as the square of the peak amplitude of the electric field, E_0^2. The transition to the nonlinear regime appears to occur for $10^8 < E_0 < 10^9$ V/m. Crucially, by changing the polarization ϕ of the laser field, we can tune M_z at saturation within a wide range of values: maximum for $\phi = \pm 90°$ (circular polarization) and zero for $\phi = 0°$ (linear polarization). One can also flip the direction of M_z by changing the polarization by an angle of 180°. After the perturbation is switched-off, the induced magnetic moment does not decay in our calculations owing to the high symmetry of the jellium systems and the absence of defects and phonon scattering.

A detailed spatial analysis of the induced electron density and the current density shows that, the primary contribution in building up orbital magnetic moment comes from the surface. However, significant contributions from the core of the cluster are also present. These core contributions are a direct consequences of the Friedel-like oscillations of the ground-state electron density due to quantum-mechanical size-confinement effects. They are not captured in the QHD model,[22] which lacks the orbital resolution of the electronic system.

We also presented the effect of size and of chemical species of the system (i.e., r_s) on the laser-generated magnetic dipole. For a given chemical species (i.e., constant r_s), the magnetic moment per electron remains almost constant in the size range discussed in this work (up to about ∼6.5 nm in diameter, for K), that is, M_z varies linearly with the total number of electrons. The effect of chemical species was studied for K, Na, and Au using their respective r_s values. For systems of different chemical nature having the same size or having the same number of electrons, we showed that at LSP frequency the generated magnetic moment per energy absorbed increases with the Wigner-Seitz radius r_s.

All in all, the present findings confirm the results obtained using a simpler QHD approach:[22] a sizable orbital magnetic moment can be generated in metal clusters using circularly polarized laser pulses at or near the surface plasmon frequency. However, unlike in the QHD approach where the magnetic moment is entirely due to surface contributions, the present results show that both the surface and the core of the cluster contribute to the magnetic moment. The generated orbital magnetic moment is very stable and can, in principle, persist for many tens of femtoseconds. The effect is robust when testing for different chemical species and cluster sizes.

Finally, we mention that our simulations of the generation of orbital magnetic moment in gold clusters produced results having magnitudes consistent with recently reported experimental study.[14] The decisive point for the magnetic moment generation is that the material supports a strong plasmonic response at the driving laser frequency. The robust confirmation of this magneto-plasmonic phenomenon presented here is believed to lead to novel techniques in achieving ultrafast plasmon-assisted optical switching in suitable systems such as, core/shell nanoparticles, supported gold discs, or gold rings with a magnetic core.

ASSOCIATED CONTENT

Supporting Information

The Supporting Information is available free of charge at https://pubs.acs.org/doi/10.1021/acsphotonics.0c00462.

Ground-state electron density for potassium clusters of different sizes. Effect of using a Gaussian laser pulse. Animation showing the dynamics of electrons (in a K_{561} jellium cluster at resonance) after laser is switched-off. Absorption spectra of jellium spheres with different electron densities, but having almost the same jellium radius, and the time-dependence of energy in them due to laser excitation at resonance. Absorption spectra of jellium spheres with different electron density but having the same number of electrons, and the time-dependence of energy in them due to laser excitation at resonance. Comparison of magnetic moment for gold with recent experimental findings (PDF)

AUTHOR INFORMATION

Corresponding Authors

Rajarshi Sinha-Roy − *Aix-Marseille Univ, CNRS, CINAM, 13288 Marseille, France; European Theoretical Spectroscopy Facility (ETSF);* orcid.org/0000-0002-1324-9820; Email: sinharoy@cinam.univ-mrs.fr

Giovanni Manfredi − *Université de Strasbourg, Institut de Physique et Chimie des Matériaux de Strasbourg, F-67000 Strasbourg, France*; Email: giovanni.manfredi@ipcms.unistra.fr

Authors

Jérôme Hurst − *Univ. Grenoble Alpes, CNRS, CEA, Grenoble INP, IRIG-Spintec, 38000 Grenoble, France*

Paul-Antoine Hervieux − *Université de Strasbourg, Institut de Physique et Chimie des Matériaux de Strasbourg, F-67000 Strasbourg, France*

Complete contact information is available at: https://pubs.acs.org/10.1021/acsphotonics.0c00462

Notes

The authors declare no competing financial interest.

ACKNOWLEDGMENTS

This work has used HPC resources from GENCI-IDRIS (Grant 2017-096829). R.S.-R. would like to acknowledge the contribution of the International Research Network IRN Nanoalloys (CNRS) and the in-house computational resources

in CINaM (CNRS). P.-A.H. and G.M. acknowledge fruitful discussions with M. Vomir and M. Rastei.

REFERENCES

(1) Kreibig, U.; Vollmer, M. *Optical Properties of Metal Clusters*; Springer, 1995; p 532.

(2) Stanciu, C. D.; Hansteen, F.; Kimel, A. V.; Kirilyuk, A.; Tsukamoto, A.; Itoh, A.; Rasing, Th. All-optical magnetic recording with circularly polarized light. *Phys. Rev. Lett.* **2007**, *99*, 047601.

(3) Alebrand, S.; Gottwald, M.; Hehn, M.; Steil, D.; Cinchetti, M.; Lacour, D.; Fullerton, E. E.; Aeschlimann, M.; Mangin, S. Light-induced magnetization reversal of high-anisotropy TbCo alloy films. *Appl. Phys. Lett.* **2012**, *101*, 162408.

(4) Mangin, S.; Gottwald, M.; Lambert, C.-H.; Steil, D.; Uhlir, V.; Pang, L.; Hehn, M.; Alebrand, S.; Cinchetti, M.; Malinowski, G.; Fainman, Y.; Aeschlimann, M.; Fullerton, E. E. Engineered materials for all-optical helicity-dependent magnetic switching. *Nat. Mater.* **2014**, *13*, 286−292.

(5) Lambert, C.-H.; Mangin, S.; Varaprasad, B. S. D. C. S.; Takahashi, Y. K.; Hehn, M.; Cinchetti, M.; Malinowski, G.; Hono, K.; Fainman, Y.; Aeschlimann, M.; Fullerton, E. E. All-optical control of ferromagnetic thin films and nanostructures. *Science* **2014**, *345*, 1337.

(6) El Hadri, M. S.; Pirro, P.; Lambert, C.-H.; Bergeard, N.; Petit-Watelot, S.; Hehn, M.; Malinowski, G.; Montaigne, F.; Quessab, Y.; Medapalli, R.; Fullerton, E. E.; Mangin, S. Electrical characterization of all-optical helicity-dependent switching in ferromagnetic Hall crosses. *Appl. Phys. Lett.* **2016**, *108*, 092405.

(7) John, R.; Berritta, M.; Hinzke, D.; Müller, C.; Santos, T.; Ulrichs, H.; Nieves, P.; Walowski, J.; Mondal, R.; Chubykalo-Fesenko, O.; McCord, J.; Oppeneer, P. M.; Nowak, U.; Münzenberg, M. Magnetisation switching of FePt nanoparticle recording medium by femtosecond laser pulses. *Sci. Rep.* **2017**, *7*, 4114.

(8) Vomir, M.; Albrecht, M.; Bigot, J.-Y. Single shot all optical switching of intrinsic micron size magnetic domains of a Pt/Co/Pt ferromagnetic stack. *Appl. Phys. Lett.* **2017**, *111*, 242404.

(9) Bychkov, I. V.; Kuzmin, D. A.; Tolkachev, V. A.; Plaksin, P. S.; Shavrov, V. G. Plasmon mediated inverse Faraday effect in a graphene−dielectric−metal structure. *Opt. Lett.* **2018**, *43*, 26−29.

(10) Chekhov, A. L.; Stognij, A. I.; Satoh, T.; Murzina, T. V.; Razdolski, I.; Stupakiewicz, A. Surface Plasmon-Mediated Nanoscale Localization of Laser-Driven sub-Terahertz Spin Dynamics in Magnetic Dielectrics. *Nano Lett.* **2018**, *18*, 2970−2975.

(11) Pershan, P. S.; van der Ziel, J. P.; Malmstrom, L. D. Theoretical Discussion of the Inverse Faraday Effect, Raman Scattering, and Related Phenomena. *Phys. Rev.* **1966**, *143*, 574−583.

(12) Jain, P. K.; Xiao, Y.; Walsworth, R.; Cohen, A. E. Surface Plasmon Resonance Enhanced Magneto-Optics (SuPREMO): Faraday Rotation Enhancement in Gold-Coated Iron Oxide Nanocrystals. *Nano Lett.* **2009**, *9*, 1644−1650.

(13) Maccaferri, N.; Berger, A.; Bonetti, S.; Bonanni, V.; Kataja, M.; Qin, Q. H.; van Dijken, S.; Pirzadeh, Z.; Dmitriev, A.; Nogués, J.; Åkerman, J.; Vavassori, P. Tuning the Magneto-Optical Response of Nanosize Ferromagnetic Ni Disks Using the Phase of Localized Plasmons. *Phys. Rev. Lett.* **2013**, *111*, 167401.

(14) Cheng, O. H.-C.; Son, D. H.; Sheldon, M. Light-induced magnetism in plasmonic gold nanoparticles. *Nat. Photonics* **2020**, *14*, 365−368.

(15) Battiato, M.; Barbalinardo, G.; Oppeneer, P. M. Quantum theory of the inverse Faraday effect. *Phys. Rev. B: Condens. Matter Mater. Phys.* **2014**, *89*, 014413.

(16) Kundu, A.; Zhang, S. Effect of laser induced orbital momentum on magnetization switching. *J. Magn. Magn. Mater.* **2018**, *454*, 165−169.

(17) Scheid, P.; Malinowski, G.; Mangin, S.; Lebègue, S. Ab initio theory of magnetization induced by light absorption in ferromagnets. *Phys. Rev. B: Condens. Matter Mater. Phys.* **2019**, *100*, 214402.

(18) Scholl, C.; Vollmar, S.; Schneider, H. C. Off-resonant all-optical switching dynamics in a ferromagnetic model system. *Phys. Rev. B: Condens. Matter Mater. Phys.* **2019**, *99*, 224421.

(19) Berritta, M.; Mondal, R.; Carva, K.; Oppeneer, P. M. Ab Initio Theory of Coherent Laser-Induced Magnetization in Metals. *Phys. Rev. Lett.* **2016**, *117*, 137203.

(20) Nadarajah, A.; Sheldon, M. T. Optoelectronic phenomena in gold metal nanostructures due to the inverse Faraday effect. *Opt. Express* **2017**, *25*, 12753.

(21) Koshelev, K. L.; Kachorovskii, V. Y.; Titov, M. Resonant inverse Faraday effect in nanorings. *Phys. Rev. B: Condens. Matter Mater. Phys.* **2015**, *92*, 235426.

(22) Hurst, J.; Oppeneer, P. M.; Manfredi, G.; Hervieux, P.-A. Magnetic moment generation in small gold nanoparticles via the plasmonic inverse Faraday effect. *Phys. Rev. B: Condens. Matter Mater. Phys.* **2018**, *98*, 134439.

(23) Manfredi, G. How to model quantum plasmas. *Fields Institute Communications* **2005**, *Series 46*, 263−287.

(24) Vladimirov, S. V.; Tyshetskiy, Y. O. On description of a collisionless quantum plasma. *Phys.-Usp.* **2011**, *54*, 1243−1256.

(25) Ciracì, C.; Della Sala, F. Quantum hydrodynamic theory for plasmonics: Impact of the electron density tail. *Phys. Rev. B: Condens. Matter Mater. Phys.* **2016**, *93*, 205405.

(26) Crouseilles, N.; Hervieux, P.-A.; Manfredi, G. Quantum hydrodynamic model for the nonlinear electron dynamics in thin metal films. *Phys. Rev. B: Condens. Matter Mater. Phys.* **2008**, *78*, 155412.

(27) Toscano, G.; Straubel, J.; Kwiatkowski, A.; Rockstuhl, C.; Evers, F.; Xu, H.; Asger Mortensen, N.; Wubs, M. Resonance shifts and spill-out effects in self-consistent hydrodynamic nanoplasmonics. *Nat. Commun.* **2015**, *6*, 7132.

(28) Mullins, S.-M.; Weissker, H. C.; Sinha-Roy, R.; Pelayo, J. J.; Garzón, I. L.; Whetten, R. L.; López-Lozano, X. Chiral symmetry breaking yields the I-Au60 perfect golden shell of singular rigidity. *Nat. Commun.* **2018**, *9*, 3352.

(29) Sinha-Roy, R.; García-González, P.; Weissker, H.-C. How metallic are noble-metal clusters? Static screening and polarizability in quantum-sized silver and gold nanoparticles. *Nanoscale* **2020**, *12*, 4452−4458.

(30) Yabana, K.; Bertsch, G. F. Time-dependent local-density approximation in real time. *Phys. Rev. B: Condens. Matter Mater. Phys.* **1996**, *54*, 4484−4487.

(31) Yabana, K.; Nakatsukasa, T.; Iwata, J.-I.; Bertsch, G. F. Real-time, real-space implementation of the linear response time-dependent density-functional theory. *Phys. Status Solidi B* **2006**, *243*, 1121−1138.

(32) Lermé, J. Introduction of quantum finite-size effects in the Mie's theory for a multilayered metal sphere in the dipolar approximation: Application to free and matrix-embedded noble metal clusters. *Eur. Phys. J. D* **2000**, *10*, 265−277.

(33) Hervieux, P.-A.; Benabbas, A.; Halté, V.; Bigot, J.-Y. Electronic temperature effects onthe optical response of silver nanoparticles. *Eur. Phys. J. D* **2003**, *24*, 185−189.

(34) Marques, M. A.; Castro, A.; Bertsch, G. F.; Rubio, A. octopus a first-principles tool for excited electron-ion dynamics. *Comput. Phys. Commun.* **2003**, *151*, 60−78.

(35) Bréchignac, C.; Cahuzac, P.; Leygnier, J.; Sarfati, A. Optical response of large lithium clusters: Evolution toward the bulk. *Phys. Rev. Lett.* **1993**, *70*, 2036−2039.

(36) de Heer, W. A. The physics of simple metal clusters: experimental aspects and simple models. *Rev. Mod. Phys.* **1993**, *65*, 611−676.

(37) Brack, M. The physics of simple metal clusters: self-consistent jellium model and semiclassical approaches. *Rev. Mod. Phys.* **1993**, *65*, 677−732.

(38) Lang, N. D.; Kohn, W. Theory of Metal Surfaces: Charge Density and Surface Energy. *Phys. Rev. B* **1970**, *1*, 4555−4568.

(39) Hertel, R. Theory of the inverse Faraday effect in metals. *J. Magn. Magn. Mater.* **2006**, *303*, L1−L4.

https://dx.doi.org/10.1021/acsphotonics.0c00462
ACS Photonics 2020, 7, 2429−2439